

## The Bolometric Bond Albedo of Enceladus

Liming Li<sup>a,\*</sup>, Larry Guan<sup>a</sup>, Sherry Li<sup>b</sup>, Cindy Luu<sup>a</sup>, Kevin Heng<sup>c</sup>, Patrick M. Fry<sup>d</sup>,  
Ellen C. Creedy<sup>e</sup>, Xinyue Wang<sup>e</sup>, Ronald J. Albright<sup>e</sup>, Thishan D. Karandana G.<sup>e</sup>, Xun Jiang<sup>e</sup>,  
Robert A. West<sup>f</sup>, Conor A. Nixon<sup>g</sup>, Matthew E. Kenyon<sup>f</sup>, Amanda Hendrix<sup>h</sup>, Ulyana Dyudina<sup>i</sup>

<sup>a</sup> Department of Physics, University of Houston, Houston, TX 77004, United States of America

<sup>b</sup> McLean High School, McLean, VA, 22101, United States of America

<sup>c</sup> Center for Space and Habitability, University of Bern, Bern CH-3012, Switzerland

<sup>d</sup> Space Science and Engineering Center, University of Wisconsin-Madison, Madison, WI 53706, United States of America

<sup>e</sup> Department of Earth and Atmospheric Sciences, University of Houston, Houston, TX 77004, United States of America

<sup>f</sup> Jet Propulsion Laboratory, California Institute of Technology, Pasadena, CA 91109, United States of America

<sup>g</sup> NASA Goddard Space Flight Center, Greenbelt, MD 20771, United States of America

<sup>h</sup> Planetary Science Institute, Tucson, AZ 85719, United States of America

<sup>i</sup> Space Science Institute, Boulder, CO 80301, United States of America

### ARTICLE INFO

#### Keywords:

Enceladus  
Bond albedo  
Jet plume  
Radiation budget  
Internal heat

### ABSTRACT

The bolometric Bond albedo is a fundamental parameter of planets and moons. Here, combined observations from the Cassini spacecraft and the Hubble Space Telescope are used to determine the bolometric Bond albedo of Enceladus. We provide the full-disk reflectance of Enceladus across all phase angles ( $0^\circ$ – $180^\circ$ ) from 150 nm to 5131 nm, a spectral range that accounts for nearly all incoming solar power. Considering the distribution of the monochromatic Bond albedo over wavelength, we find a value of  $0.76 \pm 0.03$  for Enceladus' bolometric Bond albedo. The corresponding optical characteristics (e.g., geometric albedo and phase function), which are closely related to Enceladus' surface properties, are also investigated. The wavelength-dependent nature of Enceladus' Bond albedo suggests that the bolometric Bond albedos of other icy moons, if they are mainly determined by the visible observations only, should be carefully considered. Our new measurements of bolometric Bond albedo can be used to better determine the radiant energy budget of Enceladus and further constrain the internal heat flow, a critical driving force for the water plumes on Enceladus.

### 1. Introduction

Ejecta plumes composed of liquid water and/or solid ice were discovered in the southern polar region of Enceladus by the Cassini spacecraft in 2005 (e.g., Porco et al., 2006; Spencer et al., 2006; Hansen et al., 2006). Enceladus is a relatively small moon with a diameter  $\sim 504.2$  km (Thomas, 2010), yet these surprisingly large plumes can reach a few hundred kilometers in height. The plumes have made Enceladus an object of great scientific interest as they may contain biomarkers for past or present life in the interior of Enceladus (e.g., McKay et al., 2008). In a recent report for the decadal strategy for planetary science and astrobiology 2023–2032 from the National Academies of Sciences, Engineering, and Medicine, an orbiter-lander for Enceladus is identified as NASA's second-highest priority flagship mission (National Academies of Sciences, Engineering, and Medicine, 2022).

To better understand the mechanism behind the plumes on Enceladus, some models (e.g., Gioia et al., 2007; Brilliantov et al., 2008) have been proposed in which the internal heat flow plays a crucial role in the eruption of the plumes. One way of estimating the heat flow is the radiant energy budget, which is defined as the balance between the emitted thermal energy and the absorbed solar energy. The radiant energy budget plays a crucial role in determining the thermal structure and related interior characteristics of Enceladus. The thermal radiance from Enceladus has been previously analyzed to determine the emitted thermal energy from the polar region where the jet plumes were discovered (Spencer et al., 2006; Howett et al., 2011). The key parameter to measure the absorbed solar energy is the bolometric Bond albedo, which is defined as the ratio between the reflected solar energy in all directions and the total incoming solar energy. Once the bolometric Bond albedo is measured, we can subtract the reflected solar energy

\* Corresponding author.

E-mail address: [lli7@central.uh.edu](mailto:lli7@central.uh.edu) (L. Li).

<https://doi.org/10.1016/j.icarus.2023.115429>

Received 25 September 2022; Received in revised form 27 December 2022; Accepted 5 January 2023

Available online 11 January 2023

0019-1035/© 2023 Elsevier Inc. All rights reserved.

from the total incoming solar energy to get the absorbed solar energy. The difference between the emitted thermal energy and absorbed solar energy can be used to constrain the internal heat flow, which is probably the main driver for the water plumes on this moon.

The albedo-related optical characteristics can help us to understand the surface properties of Enceladus (e.g., Buratti and Veverka, 1984; Verbiscer et al., 1990, 2005, 2006). In particular, the shape of the Enceladus' spectra from ultraviolet to near infrared can be used to examine the surface composition and regolith grain size (e.g., Emery et al., 2005; Filacchione et al., 2007). A good review of our current understanding of Enceladus' surface properties from spectroscopy is provided by Postberg et al. (2018). Enceladus' bolometric Bond albedo has been estimated in some previous studies (see Table 1). Visible observations with partial coverage of phase angle and/or wavelength have been used to directly characterize Enceladus' bolometric Bond albedo (e.g., Buratti and Veverka, 1984; Verbiscer and Veverka, 1994; Pitman et al., 2010). In addition, infrared observations have been used to indirectly estimate Enceladus' bolometric Bond albedo by assuming radiant energy balance (e.g., Hanel et al., 1982) or relating surface properties to observed thermal characteristics (e.g., Spencer et al., 2006; Howett et al., 2010). However, differences have emerged in previous estimates of Enceladus' bolometric Bond albedo (see Table 1). In this study, we combine as many high-quality observations as possible to re-evaluate Enceladus' bolometric Bond albedo.

Multi-instrument observations of Enceladus from the Cassini spacecraft are better suited for this purpose than other observations because

**Table 1**  
Measurements and observations of Enceladus' bolometric Bond albedo.

| Bolometric Bond Albedo | Observations  | References   |
|------------------------|---|--|
| 0.89 ± 0.02            | Voyager IRIS observations (wavelength: ~10–50 μm)   | Hanel et al. (1982)  |
| 0.9 ± 0.1              | Voyager ISS & ground-based observations (wavelengths: ~ 480 nm, 550 nm, and 634 nm; phase angles: ~ 0.7°, 3.3–4.4°, 13–44°) | Buratti and Veverka (1984)<br>Verbiscer and Veverka (1994) |
| 0.80–0.82              | Cassini CIRS/FP3 observations (wavelengths: ~ 9–17 μm)  | Spencer et al. (2006)                                      |
| 0.81 ± 0.04            | Cassini CIRS/FP1 observations (wavelengths: ~17–1000 μm)  | Howett et al. (2010)                                       |
| 0.85 ± 0.11            | Cassini/VIMS observations (wavelengths: ~ 351–5131 nm; phase angles: ~ 1–160°)  | Pitman et al. (2010)                                       |
| 0.76 ± 0.03            | HST and Cassini multi-instrument (ISS, UVIS, and VIMS) observations (wavelengths: ~150–5131 nm; phase angles: ~ 0.2–175°)   | This work  |

Note: The full names of the abbreviations in the table are introduced as below. The IRIS and ISS are two instruments on the Voyager spacecraft. They are Infrared Interferometer Spectrometer and Radiometer (IRIS) and Imaging Science Subsystem (ISS), respectively. The CIRS, ISS, VIMS, and UVIS are four instruments on the Cassini spacecraft. They are Composite Infrared Spectrometer (CIRS), Imaging Science Subsystem (ISS), the Visual and Infrared Mapping Spectrometers (VIMS), and Ultraviolet Imaging Spectrograph (UVIS), respectively. Enceladus' bolometric Bond albedo from the infrared observations recorded by the Voyager/IRIS and Cassini/CIRS (Hanel et al., 1982; Spencer et al., 2006; Howett et al., 2010) are indirect estimates by radiant energy balance (Hanel et al., 1982) or the relationship between observed thermal characteristic and surface properties (e.g., bolometric Bond albedo) (Spencer et al., 2006; Howett et al., 2010). For the estimates based on Cassini/CIRS observations, Spencer et al. (2006) used the observations recorded by the CIRS focal plane 3 (FP3 ~ 9.1–16.7 μm). A follow-up study (Howett et al., 2011) used the observations recorded by the CIRS focal plane 1 (FP1 ~ 16.7–1000 μm) because Enceladus' emitted power concentrates more in the FP1 wavelengths (~ 90%) than in the FP3 wavelengths (~ 10%). The HST stands for Hubble Space Telescope. For more details of the observations used in this study, please also see Table 2.

they have many advantages (e.g., much better coverage of wavelength and phase angle) (see more details in the data sections). However, using data from only a single Cassini instrument has serious drawbacks. For example, the Cassini Ultraviolet Imaging Spectrograph (UVIS) (Esposito et al., 2004) and Imaging Science Subsystem (ISS) (Porco et al., 2004) have substantial limitations in the wavelength coverage available for measuring the reflected solar radiance. On the other hand, while the Visual and Infrared Mapping Spectrometer (VIMS) (Brown et al., 2004) has relatively better coverage of wavelength, it suffers from incomplete coverage of phase angle for available observations with relatively high spatial resolution (see sections 3 and 4). Therefore, a combination of Cassini observations from multiple instruments, which is supplemented by observations from other missions, is used in this work to measure the bolometric Bond albedo of Enceladus.

## 2. Methodology

The methodology of computing the bolometric Bond albedo was described in some previous studies (Conrath et al., 1989; Hanel et al., 2003; Li et al., 2018; Creecy et al., 2021). The bolometric Bond albedo  $A$  is defined as the ratio between the reflected solar power  $P_{reflect}$  and the incident solar power  $P_{incident}$ . For the full-disk measurements, the incident solar power  $P_{incident}$  is determined immediately once the distance between Enceladus and the Sun is known. The full-disk incident solar power can be expressed as  $P_{incident} = \int_{\lambda_1}^{\lambda_2} \pi F(\lambda) d\lambda$ , where  $\pi F(\lambda)$  is the solar power over the whole disk of Enceladus at a given wavelength  $\lambda$  and  $F(\lambda)$  is the full-disk solar spectral intensity. The solar power over the whole disk of Enceladus at a given wavelength ( $\pi F(\lambda)$ ) can be computed by the product of the Spectral Solar Irradiance (SSI) at Enceladus and the total area of Enceladus' full disk. We construct the SSI at Enceladus by dividing the observed SSI at Earth by the squared distance between the Sun and Enceladus in units of AU (see section 3.1 for details). The full-disk reflected solar power  $P_{reflect}$  is a measure of the solar radiance reflected by Enceladus' disk into all directions and at all wavelengths. Assuming that this quantity is independent of azimuth angle (Conrath et al., 1989), we have the full-disk reflected solar power as  $P_{reflect} = 2\pi \int_{\lambda_1}^{\lambda_2} \int_0^\pi I_\lambda(g) \sin(g) dg d\lambda$ , where  $g$  is the phase angle (i.e., the angle between the line from the Sun to Enceladus and the line from the observer to Enceladus) and  $I_\lambda(g)$  represents the full-disk reflected spectral intensity. The full-disk reflected spectral intensity  $I_\lambda(g)$  can be computed as the product of the reflected solar radiance and the area of Enceladus' disk at a given wavelength  $\lambda$  and phase angle  $g$ . Then the bolometric Bond albedo  $A$  can be expressed as

$$A = \frac{P_{reflect}}{P_{incident}} = \frac{2 \int_{\lambda_1}^{\lambda_2} \int_0^\pi I_\lambda(g) \sin(g) dg d\lambda}{\int_{\lambda_1}^{\lambda_2} F(\lambda) d\lambda} \quad (1)$$

We first discuss the Bond albedo at a given wavelength (i.e., the monochromatic Bond albedo). The monochromatic Bond albedo can be expressed as  $A(\lambda) = 2 \int_0^\pi I_\lambda(g) \sin(g) dg / F(\lambda)$ . Introducing the full-disk reflected solar spectral intensity at 0° phase angle ( $I_\lambda(0)$ ), we can rewrite the monochromatic Bond albedo as

$$A(\lambda) = \frac{2 \int_0^\pi I_\lambda(g) \sin(g) dg}{F(\lambda)} = \frac{I_\lambda(0)}{F(\lambda)} \left[ 2 \int_0^\pi \frac{I_\lambda(g)}{I_\lambda(0)} \sin(g) dg \right] \quad (2)$$

We set the first factor in Eq. (2) as  $A_0(\lambda) = I_\lambda(0)/F(\lambda)$ , which is the monochromatic geometric albedo (Conrath et al., 1989; Li et al., 2018). We also define the full-disk reflectance ( $A_g(\lambda)$ ) as the ratio between the full-disk reflected spectral intensity ( $I_\lambda(g)$ ) and the full-disk solar spectral intensity ( $F(\lambda)$ ), which is expressed as  $A_g(\lambda) = I_\lambda(g)/F(\lambda)$ . The ratio between the full-disk reflected spectral intensity at different phase angles ( $I_\lambda(g)$ ) and the full-disk reflected spectral intensity at 0° phase angle ( $I_\lambda(0)$ ) is the integral phase function (“phase function” in brief), which is represented by  $r(g)$  (i.e.,  $r(g) = I_\lambda(g)/I_\lambda(0)$ ) (Conrath et al., 1989; Li et al., 2018).

We further define one factor in Eq. (2) as  $q(\lambda) = 2 \int_0^\pi [I_\lambda(g)/I_\lambda(0)] \sin(g) dg$ . The variable  $q(\lambda)$  is the monochromatic phase integral (Conrath et al., 1989; Li et al., 2018), which is the integral of phase function ( $r(g)$ ) over phase angle. Introducing  $F(\lambda)$  into the phase integral, we have  $q(\lambda) = 2 \int_0^\pi \{ [I_\lambda(g)/F(\lambda)] / [I_\lambda(0)/F(\lambda)] \} \sin(g) dg = 2 \int_0^\pi [A_g(\lambda)/A_0(\lambda)] \sin(g) dg$ . Therefore, the variable  $q(\lambda)$  also represents an integral of the ratio between the reflectance and the geometric albedo over phase angle. Then we can express the monochromatic Bond albedo  $A(\lambda)$  as the product of the monochromatic geometrical albedo and the phase integral ( $A(\lambda) = A_0(\lambda)q(\lambda)$ ).

Now, we discuss how to determine the wavelength-averaged Bond albedo (i.e., the bolometric Bond albedo) from the monochromatic bond albedo. We approximate the integration of wavelength with a sum in Eq. (1) because we have measurements at discrete wavelengths. In this study, we investigate the monochromatic Bond albedo with a spectral resolution of 1 nm ( $\Delta\lambda=1$  nm). With a suitable conversion and substituting the monochromatic Bond albedo ( $A(\lambda)$ ) into Eq. (1), we quantify the bolometric Bond albedo as

$$A = \frac{\sum_\lambda F(\lambda)A(\lambda)\Delta\lambda}{\sum_\lambda F(\lambda)\Delta\lambda} = \sum_\lambda \frac{F(\lambda)}{\sum_\lambda F(\lambda)} A(\lambda) = \sum_\lambda W(\lambda)A(\lambda) \quad (3)$$

where  $W(\lambda) = F(\lambda)/\sum_\lambda F(\lambda)$ , which represents the weighting factors of SSI at different wavelengths over the total incident solar power. Once the monochromatic Bond albedo  $A(\lambda)$  at each wavelength is measured, we can then compute the bolometric Bond albedo  $A$  from knowledge of the weighting factor  $W(\lambda)$ .

### 3. Observational data sets

The SSI provides a necessary input for computing the reflected solar spectral intensity and hence monochromatic Bond albedo. In addition, we require the observations of reflected solar spectral intensity ( $I_\lambda(g)$ ) over ultraviolet, visible, and near-infrared wavelengths in which the SSI is concentrated. Observations of  $I_\lambda(g)$  should cover phase angles from  $0^\circ$  to  $180^\circ$  to enable us to determine the phase function and hence the bolometric Bond albedo. The requisite observations are mainly garnered from the multiple instruments of the Cassini spacecraft. In addition, observations recorded by ground-based observatories and Earth-orbiting telescopes (e.g., Hubble Space Telescope (HST)), which are termed as supplementary observations, can help us to validate the Cassini data and fill in observational gaps. The three datasets (i.e., SSI, Cassini observations, and supplementary observations) are introduced in this section.

#### 3.1. Data of SSI

The solar irradiance, which is an integration of SSI over wavelength, varies by  $\sim 0.1\%$  on the time scale of decades (Willson and Mordvinov, 2003; Lean and Rind, 2009). However, the SSI at some wavelengths can vary by much larger magnitudes ( $>10\%$ ) (Creedy et al., 2021). Therefore, it is better to include the temporal variations of the SSI, because the SSI is the reference for computing the Bond albedo of Enceladus in different years of the Cassini period (2004–2017). We include the SSI from 0 to 5131 nm (i.e., the longest wavelength of the Cassini/VIMS), a range that contributes about  $\sim 99.5\%$  of the total solar power. Our construction of the time variation of SSI from 2004 to 2017 is based on multiple data sets. At wavelengths from 0 nm 4000 nm, we use three SSI datasets: (1) the Solar EUV Experiment (SEE) (2004–2017) ([http://asp.colorado.edu/lisird/data/timed\\_ssi\\_13a/](http://asp.colorado.edu/lisird/data/timed_ssi_13a/)); (2) the Solar Radiation and Climate Experiment (SORCE) (2004–2017) ([https://asp.colorado.edu/lisird/data/sorce\\_ssi\\_13/](https://asp.colorado.edu/lisird/data/sorce_ssi_13/)); and (3) the American Society for Testing and Materials (ASTM) (climatology data) (<https://www.nrel.gov/grid/solar-resource/spectra-am1.5.html>) (see Table 2). We found no good datasets for the SSI from 4000 nm to 5131 nm, so we compute it

**Table 2**  
Observational Data Sets for Measuring Enceladus' Bond Albedo.

| Variables                       | Cassini Observations  | Other Observations   |
|---------------------------------|---|--|
| solar spectral irradiance (SSI) |   | SEE (wavelengths: $\sim 0$ –200 nm; time period: 2004–2017)<br>SORCE (wavelengths: $\sim 200$ –2400 nm; time period: 2004–2017)<br>ASTM (wavelengths: $\sim 2400$ –4000 nm; time period: climatology)<br>Blackbody spectrum (wavelengths: $\sim 4000$ –5131 nm)  |
| phase function                  | ISS (wavelengths: $\sim 264$ –939 nm; phase angles: $\sim 0.2$ – $175^\circ$ )<br>VIMS (wavelengths: $\sim 350$ –5131 nm; phase angles: $\sim 14$ – $152^\circ$ ) | HST/WFPC2 (wavelengths: $\sim 338$ –1022 nm; phase angles: $\sim 0.3$ – $6.5^\circ$ )<br>Voyager (wavelengths: $\sim 480$ nm; phase angles: $\sim 13$ – $44^\circ$ )<br>Ground-based telescope (wavelengths: $\sim 550$ nm, $\sim 634$ nm; phase angles: $\sim 0.7^\circ$ and $\sim 3.3$ – $4.4^\circ$ ) |
| reflectance spectra             | VIMS (wavelengths: $\sim 350$ –5131 nm; phase angle: $\sim 14$ – $152^\circ$ )<br>UVIS (wavelengths: $\sim 150$ –190 nm; phase angle: $\sim 15^\circ$ )           | HST/FOS (wavelengths: $\sim 193$ –264 nm; phase angle: $\sim 5^\circ$ )  |

Note: The full names of the abbreviations in the table are introduced as below. The ISS, VIMS, and UVIS are three instruments on the Cassini spacecraft, which are explained in Table 1 and the main text. The SEE, SORCE, and ASTM are three data sets for the solar spectral irradiance (SSI). They are the Solar EUV Experiment (SEE), the Solar Radiation and Climate Experiment (SORCE), and the American Society for Testing and Materials (ASTM), respectively. The FOS and WFPC2 represent the Faint Object Spectrograph (FOS) and the Wide Field Planetary Camera 2 (WFPC2) respectively on the Hubble Space Telescope (HST).

by assuming a blackbody spectrum for the Sun with a temperature 5778 K.

After constructing the SSI at Earth in the wavelength range 0–5131 nm during the Cassini period, we divide the SSI by the square of the distance between the Sun and Enceladus to get the SSI at Enceladus in the same period. The distance between the Sun and Enceladus during the Cassini period is taken from the NASA/JPL solar system dynamics – the Horizons Web-interface (<https://ssd.jpl.nasa.gov/horizons.cgi>). Panel A of Fig. S1 shows examples of the SSI in some years. The temporal variations of the SSI at Enceladus are mainly attributed to the significant variations of Sun-Enceladus distance due to Saturn's large orbital eccentricity around the Sun ( $\sim 0.052$ ), although the intrinsic solar variability also contributes some variation. The time-varying SSI is used to convert the reflected solar spectral intensity of Enceladus to reflectance (see section 2). Panel B of Fig. S1 shows the solar irradiance (i.e., solar flux) at Enceladus, which is a wavelength integration of SSI shown in panel A. During the Cassini epoch, the solar irradiance at Enceladus decreased by 19% from  $\sim 16.8 \text{ Wm}^{-2}$  in 2004 to  $\sim 13.6 \text{ Wm}^{-2}$  in 2017.

#### 3.2. Cassini observational data

The Cassini spacecraft conducted long-term observations of the Saturn system from October 2004 to September 2017, making many observations of Enceladus on multiple flybys. In this study, we mainly analyze the observations of Enceladus' reflected solar radiance from two Cassini instruments: ISS and VIMS. The ISS and VIMS observations offer improvements over earlier observations, which have been discussed in our previous studies (Li et al., 2010, 2011, 2012, 2015, 2018; Creedy

et al., 2019, 2021). Here, we briefly introduce the two Cassini instruments. As the imaging system of the Cassini spacecraft, the ISS is a Charged-Coupled Device with two cameras (the narrow-angle and wide-angle cameras) (Porco et al., 2004). Both cameras have multiple filters ranging from the ultraviolet to the near infrared.

We mainly used observations recorded in 12 filters from 264 nm to 939 nm to compute the full-disk Bond albedo of Enceladus. The basic characteristics of 12 filters (i.e., the three ultraviolet filters: UV1 at  $\sim 264$  nm, UV2 at  $\sim 306$  nm, and UV3 at  $\sim 343$  nm; the three methane-absorption filters: MT1 at  $\sim 619$  nm, MT2 at  $\sim 727$  nm, and MT3 at  $\sim 889$  nm; the three continuum filters: CB1 at  $\sim 635$  nm, CB2 at  $\sim 750$  nm, and CB3 at  $\sim 939$  nm; and the three colour filters: BL1 at  $\sim 455$  nm, GRN at  $\sim 569$  nm, and RED at  $\sim 649$  nm) have been previously described in the ISS overview paper (Porco et al., 2004) and are summarized in our previous study of Jupiter (Li et al., 2018).

To compute the full-disk Bond albedo, we searched for global images of Enceladus from the complete ISS datasets on the Planetary Data System (PDS) (<https://pds-imaging.jpl.nasa.gov/volumes/iss.html>). We selected ISS global images with spatial scales better than  $\sim 15$  km/pixel, which resolve Enceladus sufficiently well for our purposes, to conduct the measurements. The corresponding phase angles vary from  $\sim 0^\circ$  to  $\sim 175^\circ$ , which offer the best among all available observations. Examples of the Cassini ISS observations at different phase angles are displayed in Fig. 1. The images in Fig. 1 suggest that Enceladus' brightness (i.e., calibrated radiance) is much higher near opposition than at other phase angles. The brightness surge near  $0^\circ$  phase angle is related to the superposition of coherent backscattering and shadow-hiding opposition effects, which were discussed in some previous studies (e.g., Verbiscer et al., 1990, 2005, 2006; Verbiscer and Veverka, 1994; Verbiscer and Helfenstein, 1998; Hapke, 2002). The shadow-hiding opposition effect is caused by the fact that particles hide their own shadow at small phase angles (Hapke, 2002). The coherent backscattering is more complicated, which involves constructive interference between photons propagating along inverse paths in the medium (Hapke, 2002). Frost grains, which are aggregated into particles of complex texture producing the constructive interference of multiply scattered waves propagating along

the same light-scattering paths but in opposite directions (e.g., Verbiscer and Veverka, 1990; Mishchenko and Dlugach, 1992; Mishchenko, 1992), probably contribute to the coherent backscattering of Enceladus. In general, the coherent backscattering opposition effect is much sharper ( $\sim 1^\circ$ – $2^\circ$  wide) than the shadow-hiding opposition effect (up to  $20^\circ$  wide) in phase angle.

The Cassini ISS observations have the best coverage of phase angle, but they suffer from limited coverage of wavelength. On the other hand, the Cassini VIMS instrument was an imaging spectrometer that acquired images at 352 wavelengths between  $\sim 350$  nm and  $\sim 5131$  nm with varying spectral resolutions from  $\sim 4$  nm to  $\sim 25$  nm (Brown et al., 2004). The VIMS observations therefore extend the spectral coverage of the ISS observations. The raw global VIMS images are available on the PDS (<https://pds-imaging.jpl.nasa.gov/volumes/vims.html>). The spatial resolution is generally much lower for VIMS images than for ISS images. Here, we select the VIMS global images of Enceladus with spatial resolutions better than 50 km/pixel. The phase angle coverage is also much sparser for the VIMS observations than for the ISS observations. We searched the complete data set of the VIMS observations and found high-quality global observations with phase angles varying from  $\sim 14^\circ$  to  $\sim 152^\circ$ .

The Cassini spacecraft carried another instrument that observed the reflected solar radiance of Enceladus – UVIS (Esposito et al., 2004). The UVIS was used to observe Enceladus at wavelengths from 56 nm to 190 nm, shortward of the wavelengths covered by the ISS and VIMS. The UVIS observations have been previously used to investigate Enceladus' albedo in the wavelength range from 150 nm to 190 nm (Hendrix et al., 2018). There have been some difficulties noted in retrieving Enceladus' albedo in the shortest part of the UVIS wavelength range (56–150 nm) (Ajello et al., 2008). In addition, the SSI in the wavelength range 56–150 nm occupies only  $\sim 0.006\%$  of the total solar irradiance. Therefore, the UVIS observations in this range were not included in this study. Instead, we used Enceladus' geometric albedo data from 150 nm to 190 nm provided by a previous study (Hendrix et al., 2018), as shown in Fig. S2 of Supplementary Materials. Fig. S2 also shows the data recorded by the HST, which are introduced in the following section.

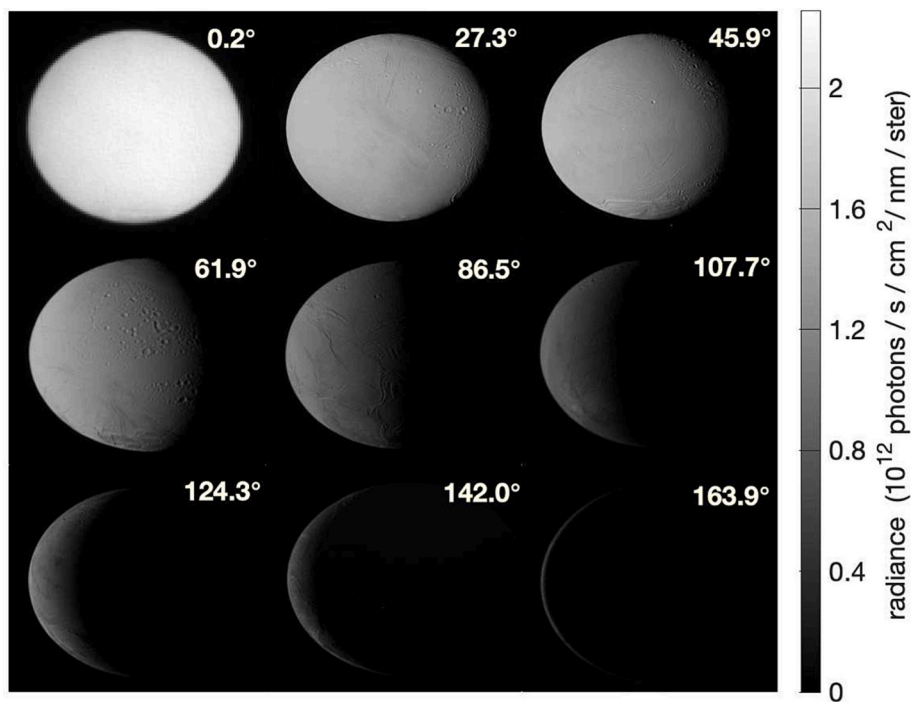


Fig. 1. Examples of Enceladus' global images at the indicated phase angles. The images were recorded by the Cassini/ISS with the Green filter (GRN  $\sim 455$  nm) and calibrated by the latest version of the ISS software. The nine images have observational times in a period of 2005–2017 and spatial scales in a range of 0.7–5.8 km/pixel. (For interpretation of the references to colour in this figure legend, the reader is referred to the web version of this article.)

### 3.3. Data of supplementary observations

In addition to the Cassini datasets, we also use other observations, which can help use to validate the Cassini measurements and fill in observational gaps. In this study, we mainly use the supplementary observations with relatively high spatial and spectral resolutions. The first of these come from the HST. Based on the observations recorded by the HST Space Telescope Imaging Spectrometer (STIS) and Faint Object Spectrograph (FOS) (Noll et al., 1997), Hendrix et al. (2018) provided the reflectance spectra from 193 nm to 304 nm, which are displayed in Fig. S2 of Supplementary Materials. In contrast to the continuous spectra recorded by HST/FOS, the HST Wide Field Planetary Camera 2 (WFPC2) observed Enceladus at discrete wavelengths from 339 nm to 1022 nm. With these, Verbiscer et al. (2005) determined Enceladus' reflectance at seven wavelengths, as shown in Fig. S3.

The second type of supplementary observations were recorded by ground telescopes, including measurements of Enceladus' Bond albedos at 550 nm and 634 nm (Verbiscer and Veverka, 1994). It should be mentioned that the observations of the HST and ground-based observatories have phase angles  $<7^\circ$ , because Enceladus' orbital distance around the Sun ( $\sim 10$  AU) is much greater than Earth's orbit around the Sun ( $\sim 1$  AU), preventing the possibility of observations at larger phase angles. The third type of supplementary observations were recorded by the Voyager spacecraft in 1980 and 1981. Unlike the observations by the HST and ground-based telescopes, the Voyager observations have much better coverage of phase angle ( $13^\circ$ – $43^\circ$ ) (e.g., Buratti and Veverka, 1984; Verbiscer and Veverka, 1994). Enceladus' reflectance based on the Voyager observations at a clear filter (wavelength  $\sim 480$  nm) has been estimated in previous studies (Buratti and Veverka, 1984; Verbiscer and Veverka, 1994). Enceladus' reflectance retrieved from ground-based telescopes and Voyager is shown in Fig. S4 of Supplementary Materials.

In summary, we use multi-instrument observations from Cassini, supplemented by observations from HST, ground-based observatories, and Voyager, to re-examine the bolometric Bond albedo of Enceladus. The observational datasets used in this study are summarized in Table 2.

## 4. Data processing

### 4.1. Calibration of Cassini data and computation of full-disk Bond albedo

After selecting raw ISS global images from the PDS, we calibrated the recorded digital brightness number to radiance units using the latest version of the Cassini ISS CALibration software ([https://pds-imaging.jpl.nasa.gov/data/cassini/cassini\\_orbiter/coiss\\_0011\\_v4.3/](https://pds-imaging.jpl.nasa.gov/data/cassini/cassini_orbiter/coiss_0011_v4.3/)), which was developed by the ISS team (West et al., 2010; Knowles et al., 2020). Calibration uncertainties, which include many error sources (e.g., uneven bit-weighting, 2-Hz noise, dark current in the ISS cameras, bright/dark pixel pair artifacts from anti-blooming mode, flat-field artifacts), are discussed in detail in the ISS calibration papers (West et al., 2010; Knowles et al., 2020) and corrected in the calibration process. We output the calibrated global images in units of radiance. An example of ISS data calibration is shown in Fig. S5.

The calibrated radiance in Fig. S5 is combined with the SSI shown in Fig. S1 to compute the full-disk reflectance ( $A_g(\lambda)$ ) at different phase angles. The calibrated radiance at each pixel of the global images is multiplied by the projected area of the pixel over Enceladus' surface and we then sum over all pixels in the disk to get the full-disk reflected spectral intensity ( $I_r(g)$ ). We also multiply the incoming solar radiance by the total area of Enceladus' disk to get the reference full-disk solar spectral intensity ( $F(\lambda)$ ). Then we can compute the full-disk reflectance of Enceladus ( $A_g(\lambda)$ ) as the ratio between the observed full-disk reflected spectral intensity and the reference full-disk solar spectral intensity (see Section 2).

The selected VIMS global images are calibrated using calibration software developed by the VIMS Operations Team (Brown et al., 2004; McCord et al., 2004; Filacchione et al., 2007; Buratti et al., 2010; Pitman

et al., 2010). The basic calibration processes (e.g., correcting flat-field artifacts, subtracting the radiation noise from Cassini's power generators, and removing cosmic rays) have been described in previous papers (e.g., McCord et al., 2004; Filacchione et al., 2007). Here, we use the version 3.5.2.0 of United States Geological Survey Integrated Software for Imagers and Spectrometers (<https://isis.astrogeology.usgs.gov/7.0.0/UserStart/index.html>) to calibrate the VIMS data. One example of the calibrated VIMS global images is shown in Fig. S6 in Supplementary Materials, which can be used to compute the full-disk reflectance of Enceladus. It should be mentioned that the calibration software uses the SSI before the Cassini epoch (Thekaekara, 1973). Therefore, we multiply Enceladus' full-disk reflectance outputted from the calibration software by the ratio between the old SSI (Thekaekara, 1973) and the SSI in the Cassini epoch (Fig. S1) to get Enceladus' correct full-disk reflectance for the Cassini epoch.

### 4.2. Consideration of the difference between leading and trailing hemispheres

Enceladus' leading and trailing hemispheres have different optical characteristics (e.g., Verbiscer and Veverka, 1994; Verbiscer et al., 1990, 2005, 2006; Howett et al., 2010; Pitman et al., 2010; Hendrix et al., 2010, 2018). Unfortunately, the Cassini observations do not separate Enceladus' leading and trailing hemispheres very well. Fig. S7 in Supplementary Materials shows that Cassini/ISS observations, which mainly focus on the leading or trailing hemispheres respectively, have a very sparse coverage of phase angle. Therefore, they not sufficient to address the difference between the leading and trailing hemispheres. In this study, we instead use reflectance measurements from two previous studies at some ultraviolet, visible, and near-infrared wavelengths (Verbiscer and Veverka, 1994; Verbiscer et al., 2005) to address the longitudinal variations (see Fig. S8). From these, we derive correction factors for the global-average bolometric Bond albedo (Fig. S8) by considering the difference between the reflectance at each longitude and the longitude-average reflectance. In addition, we linearly interpolate/extrapolate the correction factors from these wavelengths shown in Fig. S9 to the Cassini ISS and VIMS wavelengths. It should be mentioned that this is a very rough approximation especially for these infrared wavelengths longer than 1022 nm (i.e., the longest wavelength at which longitudinal variations of Enceladus' reflectance were measured in the two previous studies).

Enceladus' reflectance also changes with latitude (e.g., Buratti and Veverka, 1984; Verbiscer and Veverka, 1994). It is even more complicated to address the latitudinal variations of Enceladus' reflectance with the Cassini observations. First, we must separate the effects of the latitudinal variations from the temporal variations due to the seasonal cycle, since different seasons have different solar-illuminated latitudes. In addition, we need to separate the latitudinal variations from the above-mentioned longitudinal variations. As we discussed in Figs. S7, the longitudinal variations of Enceladus' reflectance were not observed well by Cassini. In addition, the Cassini observations cannot be used to address the temporal variations of Enceladus' reflectance either (see Fig. S10 in the following section). This incomplete sampling of longitudinal and temporal variations therefore prevents us from exploring the latitudinal variations of Enceladus' reflectance.

### 4.3. Measurements based on the Cassini observations

Cassini conducted observations of Enceladus from 2004 to 2017. In principle, we can explore the temporal variations of Enceladus' bolometric Bond albedo. However, the coverage of phase angle for high-quality Cassini observations is too poor to compute the phase integral and hence bolometric Bond albedo for each year of the Cassini period (2004–2017) (see Fig. S10 in Supplementary Materials). In addition, we expect that Enceladus' global Bond albedo does not significantly vary at time scales such as the Cassini epoch because Enceladus is an airless

body. Therefore, we combine all ISS and VIMS observations during all years of the Cassini period (2004–2017) to explore the time-mean Bond albedo of Enceladus for the Cassini epoch.

After applying the correction factors for the longitudinal variations of Enceladus' reflectance (Fig. S9) to the Cassini measurements (section 4.1), we have the final full-disk reflectance of Enceladus. Figs. 2 and 3 display the results from the Cassini ISS and VIMS measurements, respectively. Fig. 2 suggests that Enceladus' full-disk reflectance is larger than 1 at some wavelengths where phase angle is close to zero. This is because Enceladus' full-disk reflectance ( $A_g(\lambda)$ ) is referenced to a Lambertian surface (isotropically scattering), and it can therefore be larger than 1 at some specific phase angles if the surface preferentially reflects light into these phase angles. The large reflectance near  $0^\circ$  phase angle is related to the shadow-hiding and coherent backscattering opposition effects, as we discussed above in section 3.2 (see Fig. 1). Fig. 2 also shows that Cassini/ISS observations in six filters/wavelengths (UV1, UV2, UV3, BL1, GRN, and RED) have relatively good coverage of phase angle, which will be used to compute the monochromatic phase integral and Bond albedo at these wavelengths. The other six filters/wavelengths do not have good coverage of phase angle, and they are mainly used for data validation, as discussed in the next section.

Fig. 3 shows the VIMS full-disk reflectance spectra from  $\sim 14^\circ$  to  $\sim 152^\circ$  for the wavelength range 350–5131 nm. For phase angle  $< 14^\circ$ , the VIMS data set does not include images with spatial resolutions better than 50 km/pixel. Therefore, we combine the VIMS measurements with the HST measurements at low phase angles ( $\sim 0\text{--}6^\circ$ ) (Fig. S3) to compute the monochromatic phase integral and Bond albedo at the HST wavelengths. The HST measurements presented by Verbitser et al. (2005) cover seven wavelengths from 338 nm to 1022 nm (see Fig. S3). The wavelength 338 nm is outside of the VIMS wavelength range (350–5131 nm), so we combine the HST measurements at low phase angles with the VIMS observations at relatively high phase angles only at six wavelengths (i.e., 434 nm, 549 nm, 672 nm, 798 nm, 868 nm, and 1022 nm) to get the corresponding monochromatic phase integral and Bond albedo.

#### 4.4. Validation of Cassini ISS and VIMS results

The measurements of Enceladus' reflectance based on the Cassini ISS and VIMS observations are first validated by intercomparison between the two instruments. In addition, we compare the Cassini measurements

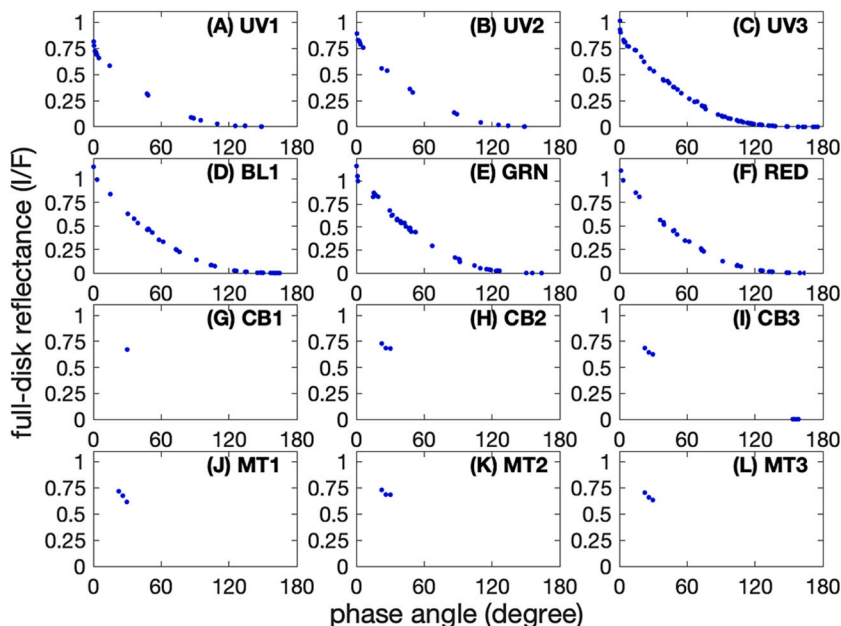


Fig. 2. Enceladus' full-disk reflectance (I/F) at different phase angles recorded by the Cassini/ISS 12 filters. (A) UV1 filter (264 nm); (B) UV2 filter (306 nm); (C) UV3 filter (343 nm); (D) BL1 filter (459 nm); (E) GRN filter (569 nm); (F) RED filter (649 nm); (G) CB1 filter (635 nm); (H) CB2 filter (750 nm); (I) CB3 filter (938 nm); (J) MT1 filter (619 nm); (K) MT2 filter (727 nm); (L) MT3 filter (889 nm). (For interpretation of the references to colour in this figure legend, the reader is referred to the web version of this article.)

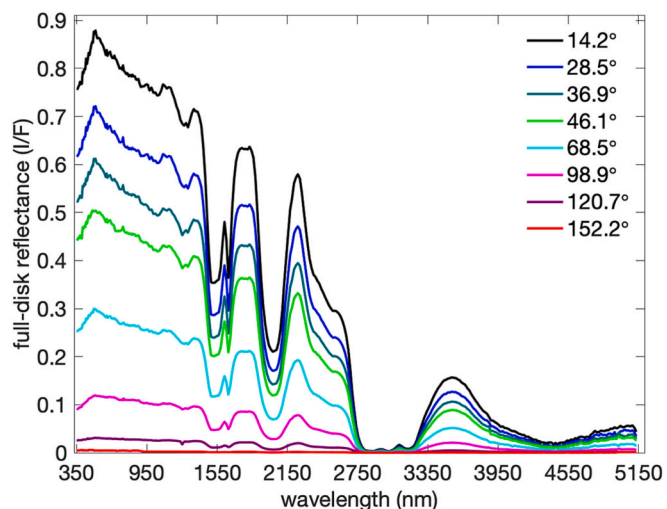


Fig. 3. Enceladus' full-disk reflectance (I/F) observed by the Cassini VIMS. By searching the whole VIMS data base, we find 21 high-quality global observations with spatial resolutions better than 50 km/pixel. The phase angles of the 21 global observations change from  $\sim 14^\circ$  to  $\sim 152^\circ$ . Here, Enceladus' full-disk reflectance at 8 different phase angles are shown as examples.

with the measurements from other observatories. Fig. 4 shows the comparison of Enceladus' full-disk reflectance between the ISS and VIMS measurements, which demonstrates that their assessments of Enceladus' full-disk reflectance are consistent. The comparison of Enceladus' reflectance at low phase angles ( $0\text{--}6.5^\circ$ ) between Cassini and other data (i.e., HST and ground-based measurements) is displayed in Fig. 5. The wavelengths of the HST and ground-based measurements are not the same as the wavelengths of the Cassini/ISS observations, so we use the closest wavelengths from the HST and ground-based observations for the comparison. Fig. 5 shows that the Cassini/ISS measurements are basically consistent with the HST and ground-based measurements.

Fig. 6 is the comparison between the Cassini and Voyager measurements for the phase angles from  $13^\circ$  to  $43^\circ$ . The Voyager reflectance shown in this figure was observed at a wavelength  $\sim 480$  nm. Cassini/VIMS also recorded Enceladus at this wavelength, while the closest ISS wavelength is the BL1 filter at  $\sim 455$  nm. Therefore, we use the Cassini/VIMS

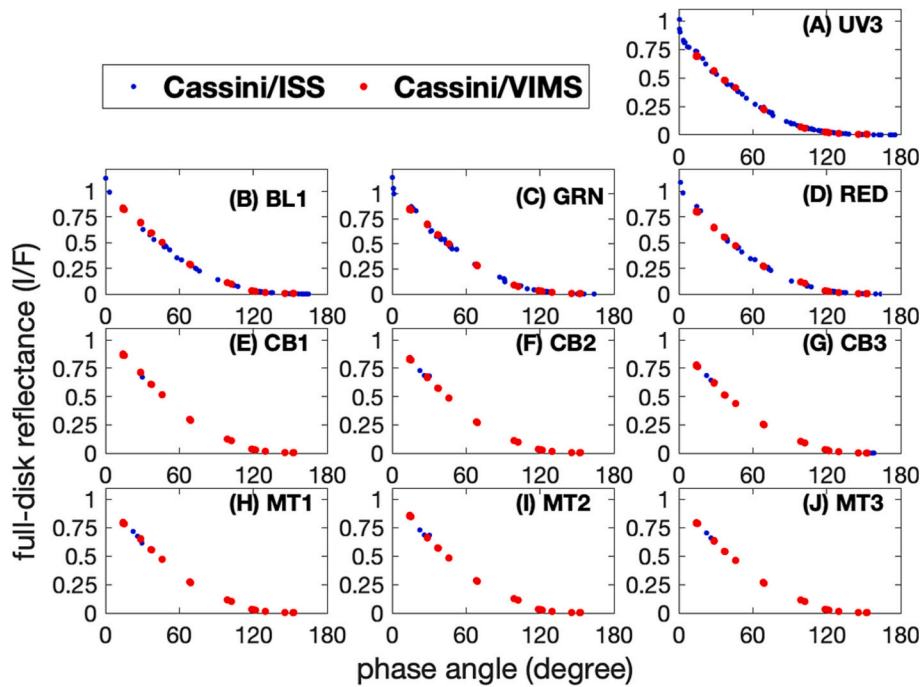


Fig. 4. Comparison of Enceladus' full-disk reflectance ( $I/F$ ) between the Cassini ISS and VIMS observations. Among the ISS 12 filters, the three ultraviolet filters (UV1  $\sim$  264 nm, UV2  $\sim$  306 nm, and UV3  $\sim$  343 nm) are out of the wavelength range of the VIMS (350–5131 nm). The wavelength of the UV3 filter (343 nm) is close to the low limit of the VIMS wavelength (350 nm), so we retain the ISS UV3 results and compare them to the VIMS measurements at 350 nm (panel A).

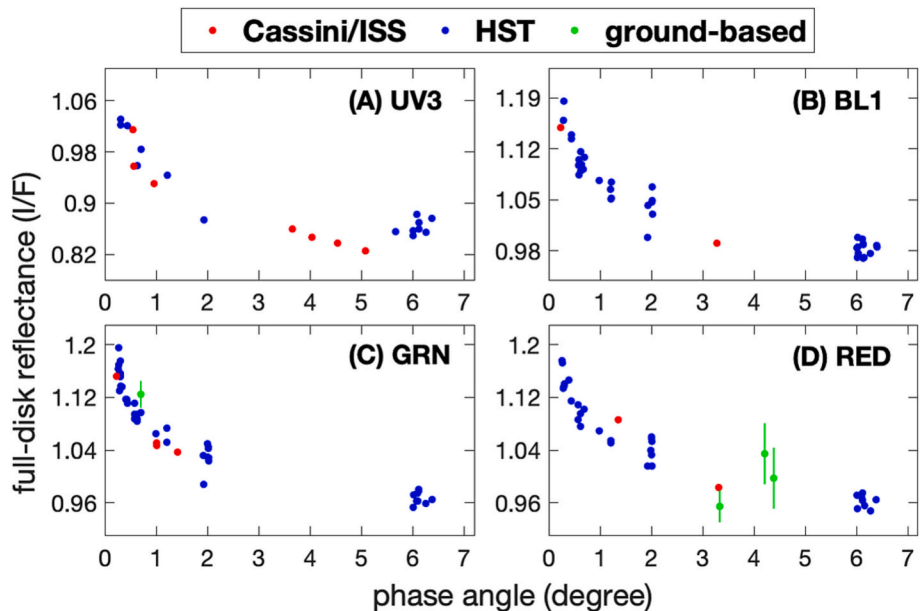


Fig. 5. Comparison of Enceladus' full-disk reflectance ( $I/F$ ) at small phase angles ( $< 7^\circ$ ) between the Cassini/ISS and the HST & ground-based measurements. The HST data are from a study by Verbiscer et al. (2005) and the ground-based data come from a study by Verbiscer and Veverka (1994).

ISS observations in the BL1 filter for the comparison in Fig. 6. This figure also suggests consistency between the Cassini measurements and the other observations.

#### 4.5. Filling observational gaps in phase angle

The Cassini/ISS observations and the combined observations from the Cassini/VIMS and HST both have good coverage of phase angle. However, these observations still have gaps in phase angle that need to be filled before computing the phase integral and Bond albedo. Hapke

(2002) developed an empirical model, which can realistically capture the coherent backscattering and shadow-hiding opposition effects. It should be mentioned that the model by Hapke (2002) was originally developed to describe the bidirectional reflectance of a planar and semi-infinite medium. For a spherical body, Hapke also developed a more complicated model to describe the phase function (Hapke, 2012).

In this work, we are mainly concerned with filling the observational gaps in phase angle and hence finding the phase integral and bolometric Bond albedo. Therefore, we simplify the phase function provided by Hapke (see Eq. (38) in Hapke, 2002) to the following expression

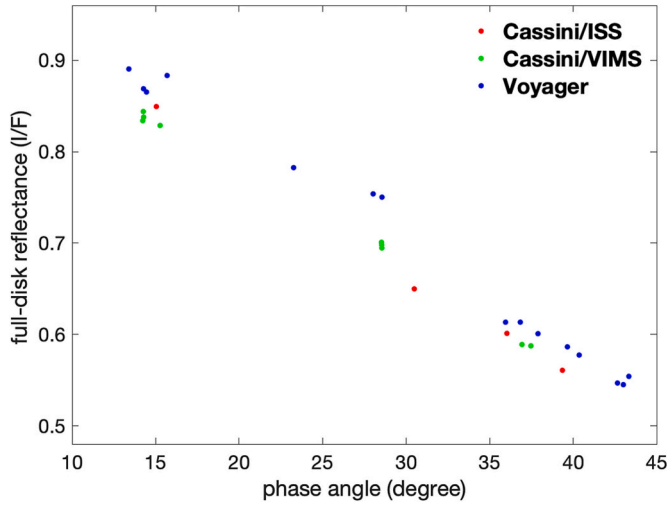


Fig. 6. Comparison of Enceladus' full-disk reflectance (I/F) at relatively high phase angles ( $\sim 13^\circ$ - $43^\circ$ ) between the Cassini measurements (ISS and VIMS) and the Voyager measurements. The Voyager observations have a wavelength 480 nm. The Cassini/ISS observations do not include that wavelength, so we use the ISS observations recorded in the BL1 filter ( $\sim 455$  nm) for the comparison. The Voyager data come from a study by Verbisser and Veverka (1994).

$$r(g) = c_1 [p(g)B_{SH}(g) + c_2]B_{CB}(g) \quad (4)$$

where  $r$  and  $g$  are phase function and phase angle respectively, as defined in section 2. The coefficient  $c_1$  represents a function of the single-scattering albedo, emission angle, and incidence angle. The coefficient  $c_2$  represents a parameter associated with emission angle and incidence angle. The expression  $p(g)$  is the single Henyey-Greenstein function (Henyey and Greenstein, 1941; Hapke, 2002), which is defined as  $p(g) = (1 - c_3^2)/(1 + 2c_3 \cos g + c_3^2)^{3/2}$ , where  $c_3$  is a coefficient related to the scattering angle. The expression  $B_{SH}(g)$  is a function for the Shadow-Hiding Opposition Effects (SHOE) (Hapke, 2002), which is defined as  $B_{SH}(g) = 1 + c_4/[1 + c_5 \tan(g/2)]$ , where the coefficient  $c_4$  is

the magnitude of the SHOE and the coefficient  $c_5$  stands for a parameter related to the extinction coefficient in the medium and the mean particle radius. The expression  $B_{CB}(g)$  describes the Coherent Backscatter Opposition Effect (CBOE) (Hapke, 2002), which is defined as  $B_{CB}(g) = 1 + c_6 B_C(g)$ , where the coefficient  $c_6$  is the magnitude of the CBOE. The expression  $B_C(g)$  is further defined as  $B_C(g) = \{1 + [1 - \exp(c_7 \tan(g/2))]/(c_7 \tan(g/2))\}/[2(1 + c_7 \tan(g/2))^2]$ , where the coefficient  $c_7$  is a parameter controlled by the wavelength and the transport mean free path in the medium.

The above discussion suggests that there are seven coefficients ( $c_1$  to  $c_7$ ) in Eq. (4). Based on Eq. (4), we use least-squares fitting (Bevington and Robinson, 2003) to obtain the fitting parameters from the observed reflectance with good coverage of phase angle. Fig. 7 shows that the simplified model works well for fitting the observed reflectance, not only at low phase angles but also at middle and high phase angles. Figs. 8 and 9 provide the fitting results for the Cassini ISS observations and the combined observations of Cassini/VIMS and HST, which also suggest that Eq. (4) works well for the observed reflectance at these wavelengths. The fitting results are used to fill the observational gaps in phase angle. It should be mentioned that our simplified equation (Eq. (4)) is used for the sole purpose of providing an empirical fit of the full-disk reflectance curve.

#### 4.6. Filling observational gaps in wavelength

After filling in the observational gaps in phase angle, we have the complete phase functions at the six filters/wavelengths (UV1  $\sim 264$  nm, UV2  $\sim 306$  nm, UV3  $\sim 343$  nm, BL1  $\sim 455$  nm, GRN  $\sim 549$  nm, and RED  $\sim 649$  nm) from the Cassini/ISS measurements (Fig. 8) and the six wavelengths (434 nm, 569 nm, 672 nm, 798 nm, 868 nm, and 1022 nm) from the combined measurements between the Cassini/VIMS and HST (Fig. 9). The above measurements only cover 12 wavelengths, and below we discuss how to fill the observational gaps in wavelength across the entire investigated spectral range.

The Cassini ISS and VIMS have observations at wavelengths different from the above 12 wavelengths, even though the coverage of phase angle in these observations is not sufficient to get the complete phase functions with Eq. (4). The complete phase functions at the 12

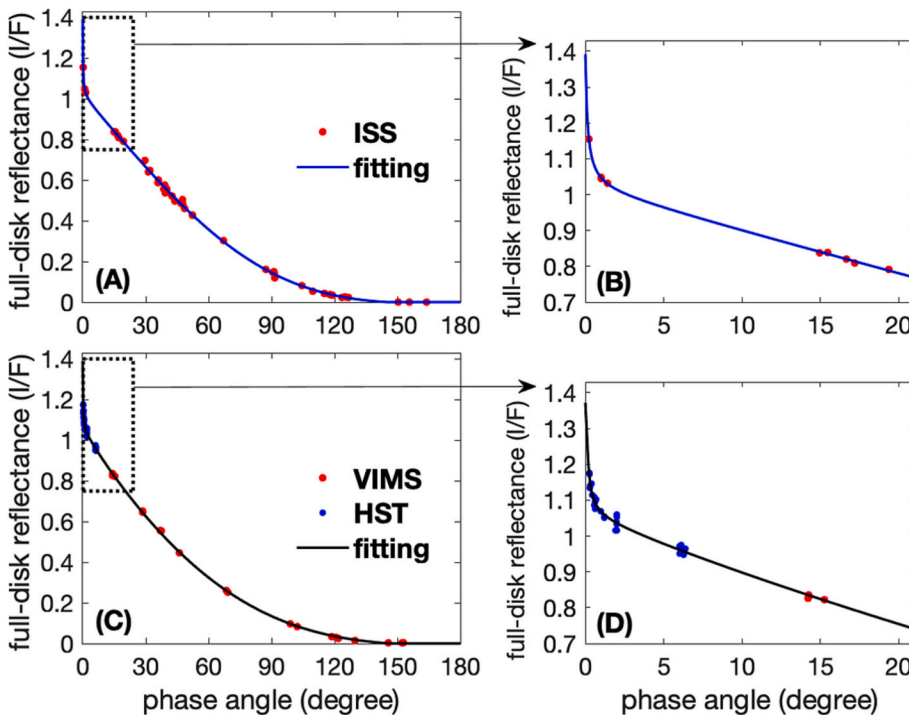


Fig. 7. Examples of fitting the phase function of Enceladus' full-disk reflectance (I/F) with Eq. (4) (see details in the text). Panel A is a fitting example for the Cassini/ISS observations at the GRN filter. Panel B is a fitting example for the combined observations between the Cassini/VIMS and HST. Panels A and C show the fitting for the complete range of phase angle ( $0^\circ$ - $180^\circ$ ). Panels B and D are the corresponding zoomed-in pictures to highlight the regions with small phase angles ( $0^\circ$ - $20^\circ$ ) for panels A and C, respectively.

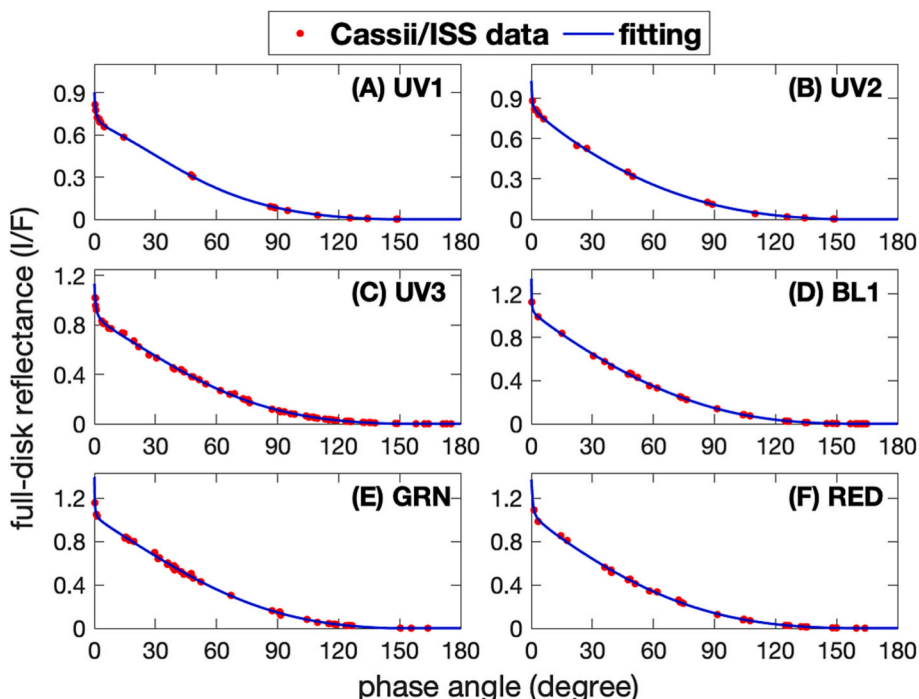


Fig. 8. Fitting results for the Cassini/ISS measurements at six filters (UV1, UV2, UV3, BL1, GRN, and RED), in which the coverage of phase angle is sufficient for the fitting. (For interpretation of the references to colour in this figure legend, the reader is referred to the web version of this article.)

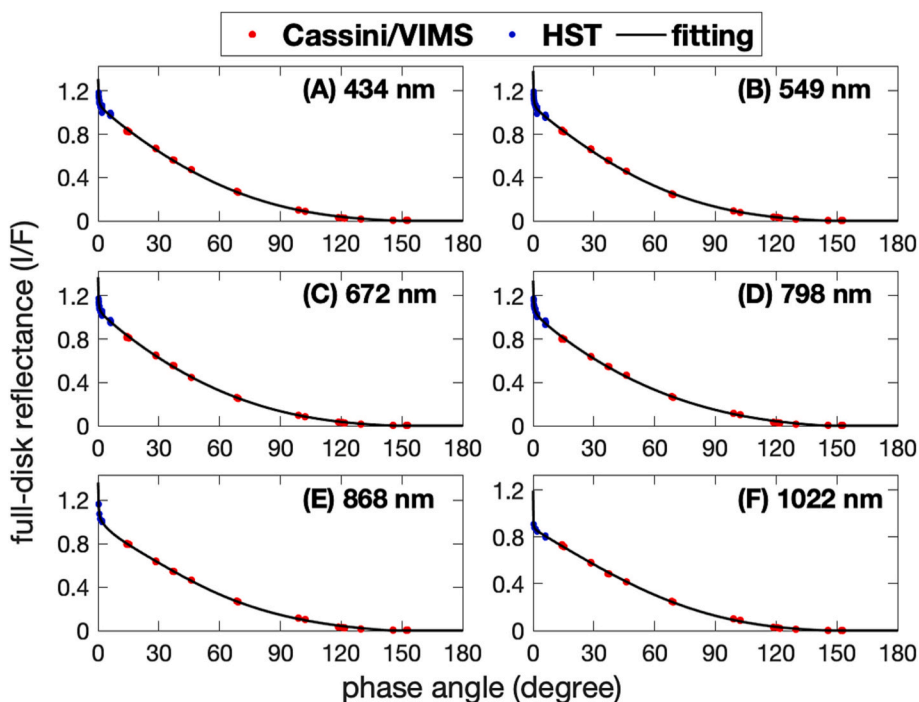
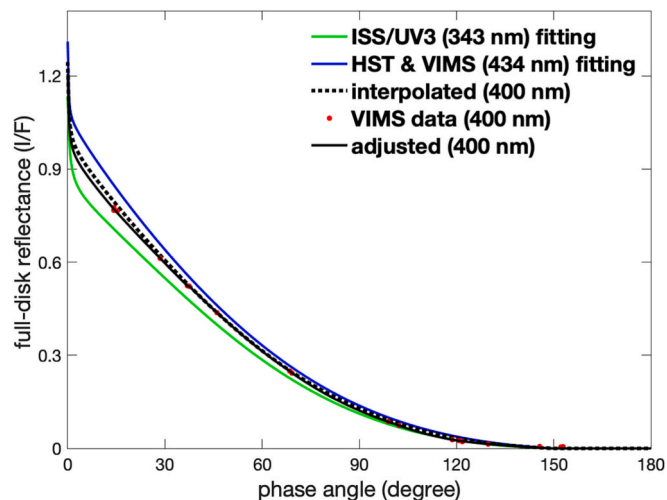


Fig. 9. Fitting results for the combined measurements between the Cassini/VIMS and HST. The HST data, which were provided in a previous study by Verbitser et al. (2005), include a wavelength 338 nm. Since this wavelength (338 nm) is beyond the low limit of the Cassini/VIMS wavelengths (350 nm), the HST data at 338 nm is not used in the fitting.

wavelengths and the available ISS/VIMS observations in other wavelengths are combined to fill the observational gaps in wavelength. For the coverage gaps from 264 nm (the shortest one of the 12 wavelengths discussed above) to 1022 nm (the longest one of the 12 wavelengths), we first linearly interpolate the complete phase functions from the 12 wavelengths to other intermediate wavelengths. Then the Cassini

observations at other wavelengths, for which the observations exist in limited phase angles only, are used to adjust the interpolated phase functions. Fig. 10 shows an example of obtaining the phase function at 400 nm, which is between the Cassini/ISS UV3 filter (343 nm) and the HST wavelength at 434 nm. For the two wavelengths one either side of 400 nm, the ISS/UV3 data can be used to get the complete phase



**Fig. 10.** An example of filling in the observational gaps in wavelength (please see discussion in the text).

function at 343 nm and the combined data between HST and VIMS can be used to get the complete phase function at 434 nm. We first linearly interpolate the complete phase functions at 343 nm (green solid line) and 434 nm (blue solid line) to the phase function at 400 nm (black dashed line). Then we use the Cassini/VIMS observed reflectance in the phase-angle range of  $\sim 14^\circ$ – $152^\circ$  to adjust the interpolated phase function. The ratio between the interpolated reflectance (black dashed line) and the VIMS-observed reflectance (red dots) at phase angle  $14^\circ$  is used to adjust the interpolated reflectance to the final reflectance (black solid line) at phase angles from  $0^\circ$  to  $14^\circ$  because there are no VIMS observations in this phase-angle interval. For the phase-angle range from  $14^\circ$  to  $29^\circ$  (i.e., the next VIMS-observed phase angle), we first compute the ratios between the interpolated reflectance and the observed reflectance at two phase angles  $14^\circ$  and  $29^\circ$ . Then we linearly interpolate the ratios from the two phase angles ( $14^\circ$  and  $29^\circ$ ) to all phase angles in the range of  $14$ – $29^\circ$ . Finally, the ratios in the range of  $14$ – $29^\circ$  are used to adjust the interpolated reflectance (black dashed line) to the final reflectance (black solid line) for the corresponding phase-angle range ( $14$ – $29^\circ$ ). Likewise, we can adjust the interpolated phase functions to the final reflectance in other phase angles. After the adjustment by the VIMS observations, we have the complete phase function at 400 nm (see black solid line in Fig. 10).

Next, we discuss the wavelengths outside of the wavelength range 264–1022 nm. For wavelengths  $< 264$  nm, we scale the phase function at 264 nm to match the observed albedo spectra from 150 nm to 264 nm. The Cassini/UVIS reflectance spectra in the wavelength range from 150 nm to 190 nm (Fig. S2) are used to fill in the observational gaps in this range. Likewise, we can use the HST reflectance spectra in the wavelength range from 193 nm to 264 nm (Fig. S2) to fill in the observational gaps in that range. For the wavelength gaps between the Cassini/UVIS and HST coverage (190–193 nm, see Fig. S2), we interpolate the phase functions at 190 nm and 193 nm to fill the phase functions from 190 nm to 193 nm.

For wavelengths longer than 1022 nm, we use the phase function at 1022 nm as a reference and use the Cassini/VIMS observed reflectance at limited phase angles in these wavelengths to obtain the phase functions. The adjustment by the Cassini/VIMS observations follows the same methodology used in Fig. 10. For the wavelengths longer than 5131 nm, we do not have suitable observational constraint. However, the SSI at wavelengths longer than 5131 nm occupies a very small fraction of the total solar flux ( $\sim 0.5\%$ ), so the phase functions in the wavelengths beyond 5131 nm are not considered in this study.

## 5. Uncertainty analysis

Enceladus' bolometric Bond albedo is determined from the monochromatic Bond albedo. The monochromatic Bond albedo is further determined by the full-disk reflected solar power and the incoming solar power at a given wavelength. The incoming solar power is mainly determined by the distance between the Sun and Enceladus (Fig. S1). Knowledge of the full-disk reflected solar power at a given wavelength and phase angle (i.e., the full-disk reflected solar spectral intensity) is based on the measurements of reflected solar radiance. Therefore, the uncertainties in the measurements of monochromatic Bond albedo mainly come from uncertainties in measuring the reflected solar radiance at different wavelengths and phase angles. We organize the uncertainty sources in the measurements of monochromatic Bond albedo into two categories: (1) the noise after calibrating the observational datasets; and (2) the uncertainty related to filling observational gaps.

We first discuss the noise related to the calibration of the ISS and VIMS data. The validation of the Cassini ISS/VIMS measurements discussed above (Figs. 4–6) suggests that the data are calibrated well. For the ISS images, we use the latest version of the Cassini ISS CALibration software (Knowles et al., 2020), to calibrate the data. The calibration process removed all known systematic errors, but there is remaining noise in the ISS calibrated data. If photon-counting statistics were the only contributor to this, the variance could be calculated by Poisson statistics of the mean photon count. However, such noise, which is probably related to point source images (stars), can in fact reach  $\pm 7$ – $10\%$  of the absolute calibrated radiance (West et al., 2010; Knowles et al., 2020). The noise for the selected global images of Enceladus in this study is smaller than that for two reasons. First, these selected high-spatial-resolution global images of Enceladus cover many pixels, so the total counts are higher than for stars that cover only a few pixels. Second, point-source images of stars have sensitivity to sub-pixel photometric nonuniformity while high-spatial resolution images of Enceladus do not. Therefore, we assume a conservative estimate ( $\sim 5\%$  of the absolute calibrated radiance) for the noise.

It should be emphasized that the noise is not systematic (Knowles et al., 2020). In other words, because of noise the real radiance is overestimated at some wavelengths and phase angles and underestimated at others (Knowles et al., 2020). When we integrate the recorded radiance over wavelength and phase angle for computing the bolometric Bond albedo, the noises at different wavelengths and phase angles cancel each other so that the net effect on the bolometric Bond albedo becomes very small ( $< 1\%$ ).

For Cassini VIMS observations, the calibration has already been discussed in a few previous studies (Brown et al., 2004; McCord et al., 2004; Filacchione et al., 2007; Pitman et al., 2010). The calibration of the VIMS data of Saturnian satellites (Pitman et al., 2010) suggests that the noise after calibration is on the order of 5% of the calibrated radiance. Based on these previous analyses, we also set 5% of the calibrated radiance as the noise level. As discussed with respect to the ISS noise, the VIMS 5% noise is not systematic either. The random noises at different wavelengths and phase can average out when integrating over wavelength and phase angle.

Our computation of Enceladus' bolometric Bond albedo also relies on the observations from Cassini/UVIS and HST (Figs. S2–S4). In this study, we mainly use the results from the previous studies (Verbiscer et al., 2005; Hendrix et al., 2018) instead of conducting a reanalysis. For simplicity, here we assume that the calibration uncertainties of the Cassini/UVIS and HST datasets have a similar magnitude as that of the calibration uncertainties in the Cassini ISS and VIMS datasets.

Now, we discuss the uncertainties related to filling observational gaps in phase angle and wavelength. We first discuss the uncertainties associated with filling observational gaps in phase angle for the 12 wavelengths in which the observations have good coverage of phase angle. Figs. 11 and 12 display the fitting residual (i.e., fitting results – observational results) for the Cassini/ISS observational data and the

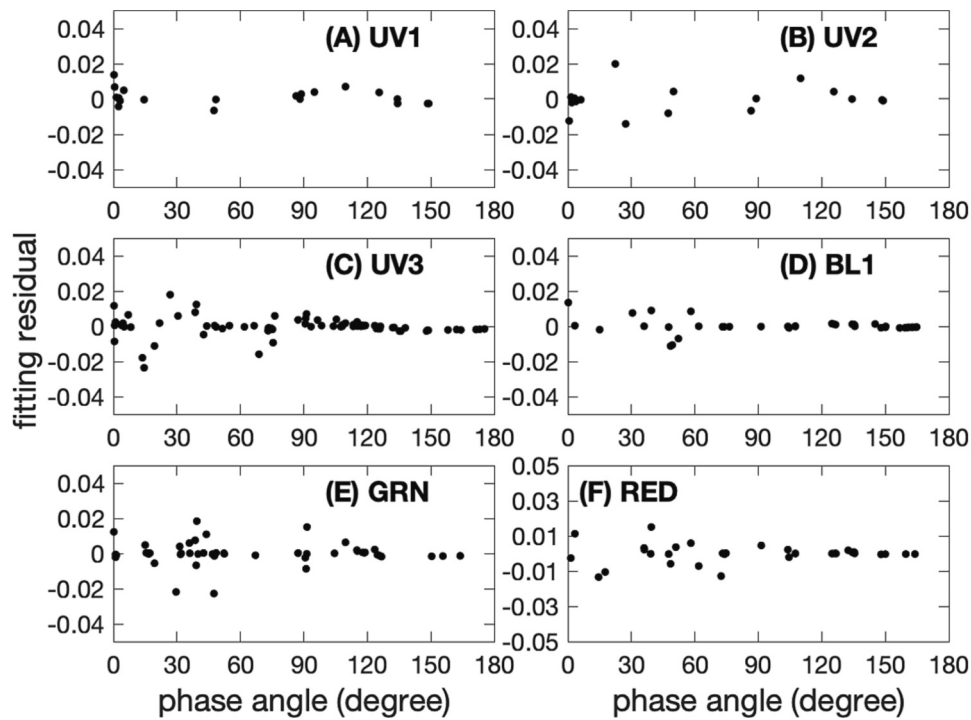


Fig. 11. Fitting residuals for the Cassini/ISS measurements at six filters, in which the coverage of phase angle is sufficient for fitting. This figure is based on Fig. 8.

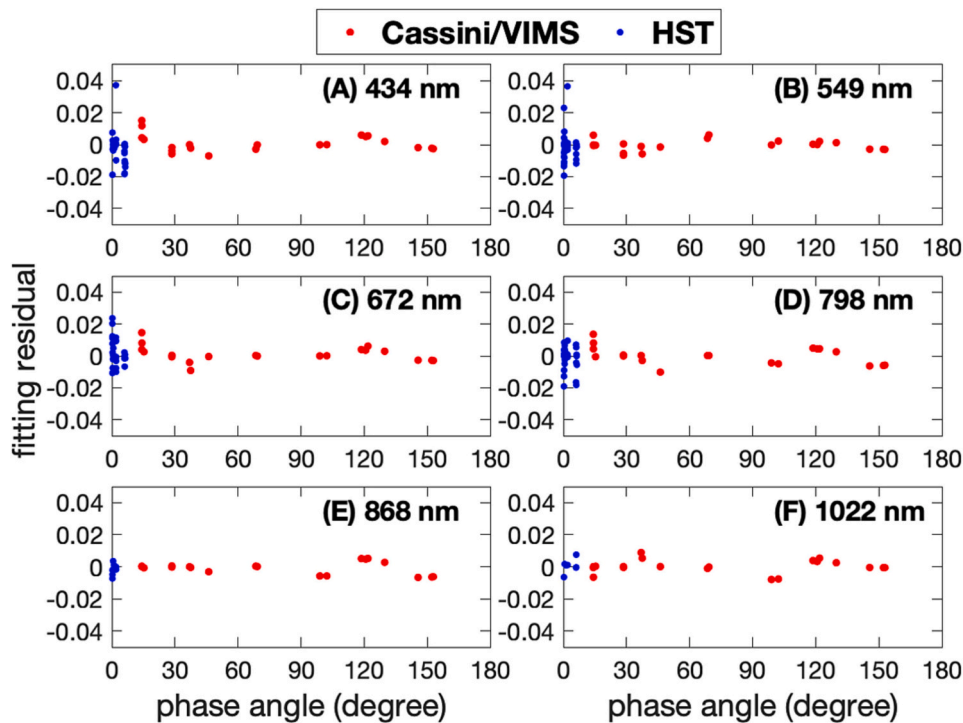


Fig. 12. Fitting residuals for the combined measurements from the Cassini/VIMS and HST. This figure is based on Fig. 9.

combined observational data from the Cassini/VIMS and HST, respectively. For estimating the uncertainties related to filling observational gaps in phase angle, we use the fitting residuals (Figs. 11 and 12), which exist in these phase angles with available measurements, to estimate the uncertainties in the observational gaps in phase angle. In other words, we interpolate and extrapolate the fitting residuals from the phase angles where observations exist to the observational gaps in phase angle for the 12 wavelengths.

Fitting residuals can be also used to evaluate how well the fitting performs. Figs. S11 and S12 in Supplementary Materials display the ratios between the fitting residuals and the observational results, which suggest that the residual ratios are <5% for most of the phase angles smaller than 100° except for a few points from the Cassini/ISS UV3 and GRN data (see panels C and E in Fig. S11). For the fittings with phase angles larger than 100°, we find that the residual ratios can be larger than 15% or even 30%. The relatively large residual ratios at large phase

angles ( $> 100^\circ$ ) are mainly because the full-disk reflectance at these large phase angles is close to zero (see Figs. 8 and 9). Considering that Enceladus' reflectance is much smaller at large phase angles ( $> 100^\circ$ ) than at other phase angles, we think that the fitting residuals at these large phase angles do not significantly affect our measurements of Enceladus' bolometric Bond albedo. However, the uncertainty related to the fitting residuals (Figs. S11 and S12) at all phase angles is considered in the analyses of the measurement uncertainties.

The fitting residuals can also be applied to estimate the uncertainties related to filling observational gaps at other wavelengths than the above 12 wavelengths. Let us take the wavelength 400 nm (Fig. 10) as an example. First, the uncertainties related to filling observational gaps in phase angle at two wavelengths (343 nm and 434 nm), which are on either sides of the wavelength 400 nm, can be estimated by the above methods. Then we linearly interpolate the estimated uncertainties at 343 nm and 434 nm to that at 400 nm and use it to estimate the uncertainty at 400 nm. To evaluate the uncertainties at the wavelengths outside of the 12 wavelengths, we simply extrapolate the uncertainties at the 12 wavelengths for the uncertainties at these wavelengths.

After addressing the two uncertainty sources (i.e., data noise and filling observational gaps) at each wavelength, we can get the total uncertainty of Enceladus' monochromatic Bond albedo. Assuming the two uncertainty sources are independent and applying the rule of error propagation of addition (Bevington and Robinson, 2003), we have the total uncertainty in each wavelength as

$$\sigma[A(\lambda)] = \sqrt{\sigma_{noise}^2(\lambda) + \sigma_{fit}^2(\lambda)} \quad (5)$$

where  $\sigma_{noise}(\lambda)$  and  $\sigma_{fit}(\lambda)$  are the uncertainties related to the data noise and fitting observational gaps respectively for the measurements after integrating the full-disk reflectance over phase angle. Based on the uncertainties in the monochromatic Bond albedo ( $\sigma[A(\lambda)]$ ), we can estimate the uncertainties of Enceladus' bolometric Bond albedo. Eq. (3) in section 2 indicates that the process of computing the bolometric Bond albedo is equivalent to the sum of the monochromatic Bond albedos at different wavelengths. Therefore, the uncertainty of Enceladus' bolometric Bond albedo is estimated from the uncertainties of

monochromatic Bond albedo by applying the rule of error propagation of addition (Bevington and Robinson, 2003).

## 6. Results

After filling in the observational gaps in phase angle and wavelength, we have Enceladus' full-disk reflectance in the two-dimensional domain of wavelength and phase angle. Fig. 13 shows that Enceladus' reflectance is much larger in the near-ultraviolet, visible, and near-infrared wavelengths (i.e.,  $\sim 200$ – $2500$  nm) than at other wavelengths (i.e.,  $< 200$  nm and  $> 2500$  nm). This figure also suggests that Enceladus' reflectance at very low phase angles ( $< 3^\circ$ ) are basically larger than 1.0 for a relatively wide wavelength range from  $\sim 300$  nm to  $\sim 1000$  nm.

Based on the reflectance shown in Fig. 13 and the methodology discussed in section 2, we can get the monochromatic geometric albedo, phase integral, and Bond albedo. Panel A of Fig. 14 shows that Enceladus' geometric albedo reaches a maximum value of  $1.41 \pm 0.08$  at 512 nm. The large geometric albedo slightly varies from its maximum 1.41 at 512 nm to 1.34 at 886 nm. Beyond this wavelength range ( $\sim 512$ – $886$  nm), the geometric albedo significantly decreases toward the shorter wavelengths ( $< 512$  nm) and the longer wavelengths ( $> 886$  nm). For the relatively long wavelengths, there are albedo dips related to water ice absorption bands (e.g.,  $\sim 1500$  nm,  $\sim 2000$  nm, and  $\sim 3000$  nm) (Filacchione et al., 2007) superposed on the large-scale decreasing trend. Panel B of Fig. 14 indicates that the phase integral varies in a small range from  $\sim 0.61$  to  $\sim 0.68$ , which is approximately consistent with previous studies (e.g., Verbiscer et al., 2005). It should be mentioned that there are no available observations of the phase functions for the wavelengths shorter than the shortest wavelength of the Cassini ISS filters (UV1  $\sim 264$  nm). Therefore, we scale the phase function at 264 nm to model the phase functions at shorter wavelengths. Considering the relatively stable phase integral, we find that the monochromatic Bond albedo (panel C) has roughly the same spectral shape as that of the geometric albedo (panel A). The monochromatic Bond albedo reaches its maximum value of 0.91 at  $\sim 579$  nm. The monochromatic Bond albedo has relatively large values oscillating between 0.85 and 0.91 in the visible and near-infrared wavelengths from

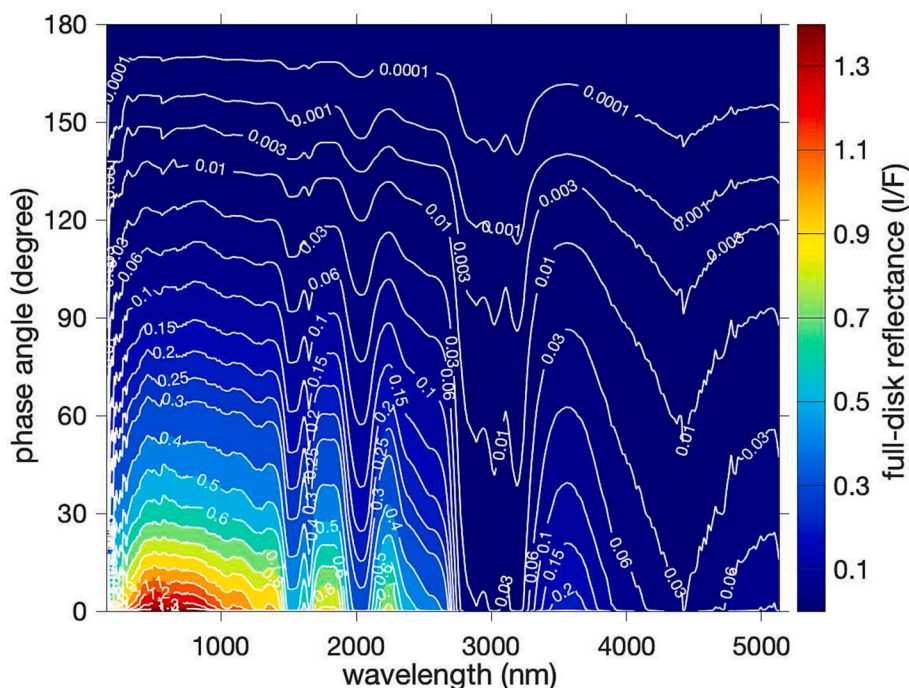
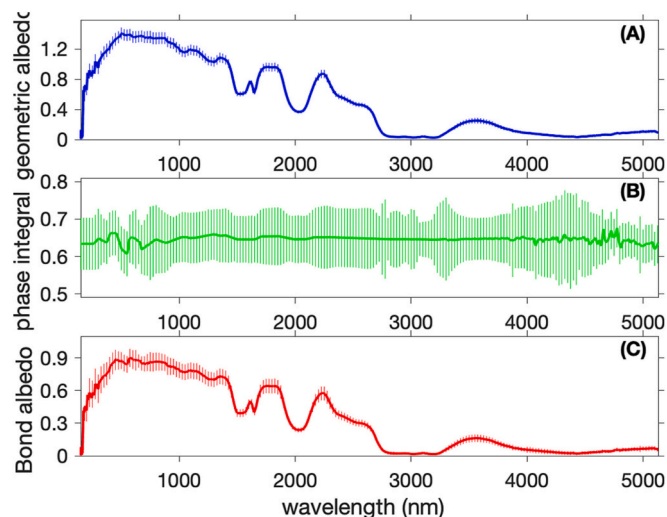


Fig. 13. Enceladus' full-disk reflectance (I/F) in the two-dimensional domain of phase angle and wavelength. The full-disk reflectance with varying phase angle ( $0^\circ$ – $180^\circ$ ) is displayed in the wavelength range of 150–5131 nm.



**Fig. 14.** Enceladus' monochromatic geometric albedo, phase integral, and Bond albedo. (A) Monochromatic geometric albedo. (B) Monochromatic phase integral. (C) Monochromatic Bond albedo. Vertical lines in the three panels represent uncertainties of measurements.

425 nm to 886 nm. Beyond this wavelength range ( $\sim 425\text{--}886\text{ nm}$ ), the monochromatic Bond albedo largely decreases except for several oscillations related to the water ice absorption bands.

The wavelength-averaged Bond albedo (i.e., the bolometric Bond albedo), which is calculated by weighting the monochromatic Bond albedo with the SSI (Eq. (3)), has a value of  $0.76 \pm 0.03$ . The new result is roughly consistent with the evaluation based on the Cassini/VIMS observations only ( $0.85 \pm 0.11$ ) (Pitman et al., 2010) and the estimate from the analysis of Enceladus' emitted power based on the Cassini thermal observations ( $0.80\text{--}0.82$  or  $0.81 \pm 0.04$ ) (Spencer et al., 2006; Howett et al., 2010) (see Table 1).

The bolometric Bond albedo ( $0.76 \pm 0.03$ ) is much smaller than the relatively large monochromatic Bond albedo in the visible and near-infrared wavelengths from 425 nm to 886 nm ( $\sim 0.85\text{--}0.91$ ). The monochromatic Bond albedo at visible wavelengths is often used as an approximation of the bolometric Bond albedo (e.g., Buratti and Veverka, 1984; Verbiscer and Veverka, 1994). The difference between the bolometric Bond albedo and the monochromatic Bond albedo at visible wavelengths suggests that such an approximation might lead to non-negligible errors. Therefore, the bolometric Bond albedos of other icy moons, if they are mainly determined by the visible observations only, should be carefully considered.

## 7. Conclusions and discussion

The Cassini multi-instrument observations, which are supplemented with other observations, are used to examine the bolometric Bond albedo of Enceladus. Enceladus' full-disk reflectance in the full range of phase angle ( $0\text{--}180^\circ$ ) from 150 nm to 5131 nm is provided. Then the global-scale monochromatic geometric albedo, phase integral, and Bond albedo in the wavelength range 150–5131 nm are derived. The geometric albedo, phase integral, and Bond albedo are fundamental optical characteristics, which can be used to better understand the surface properties of Enceladus (e.g., Buratti and Veverka, 1984; Verbiscer et al., 1990, 2005, 2006; Verbiscer and Helfenstein, 1998). The monochromatic Bond albedo in the wavelength range 150–5131 nm is further used to derive the bolometric Bond albedo of Enceladus, which has a value  $0.76 \pm 0.03$ .

Considering that Enceladus is an airless body, we may assume that Enceladus' bolometric Bond albedo at the global scale does not significantly change on seasonal timescales. Then the seasonal cycle of

Enceladus' absorbed solar power will follow that of the incoming solar flux at Enceladus. The solar power at Enceladus decreased  $\sim 19\%$  in the Cassini period (see panel B of Fig. S1). For a whole orbital period around the Sun ( $\sim 29.5$  Earth years), the temporal variation of Enceladus' solar power is beyond 20%. Therefore, we expect a strong seasonal cycle of the absorbed solar power on Enceladus. If the seasonal cycle of Enceladus' emitted power cannot exactly match that of the absorbed solar power, there will be a radiant energy imbalance on seasonal timescales, similar to that on observed Titan and Mars (Creedy et al., 2021, 2022). The measurements of the global emitted thermal power, which we will address in a future study, will help us to examine the seasonal variations of Enceladus' radiant energy budget at a global scale.

Enceladus' global radiant energy budget will help us to better understand the seasonal variations and possible long-term temporal evolution of Enceladus at a global scale. The spatial distribution of the radiant energy budget is also important. For example, the radiant energy budget in the southern polar region was used to estimate the internal heat flow (e.g., Spencer et al., 2006; Howett et al., 2011; Spencer et al., 2018), which is closely related to the plumes in the same region (e.g., Porco et al., 2006; Spencer et al., 2006; Hansen et al., 2006). In these previous studies of internal heat flow in the polar region (Spencer et al., 2006; Howett et al., 2011; Spencer et al., 2018), an estimated global-scale bolometric Bond albedo was used. The updated global bolometric Bond albedo from this study and future measurements of spatial distribution of Enceladus' bolometric Bond albedo can help us better constrain the internal heat flow on Enceladus. Measurements of regional bolometric Bond albedo can be used to compute the absorbed solar power in the polar region. In parallel, Enceladus' thermal radiance at different wavelengths, which was recorded by the different focal planes from the Cassini Composite Infrared Spectrometer (Flasar et al., 2004), has been used to estimate the emitted thermal power (Spencer et al., 2006; Howett et al., 2011; Spencer et al., 2018), the other component of the radiant energy budget. Previous studies of the emitted powers of terrestrial planets and moons (e.g., Creedy et al., 2019, 2022) suggest that the outgoing thermal radiance significantly varies with emission angle. The dependence of outgoing thermal radiance on emission angle for Enceladus has not been fully investigated yet, which should be carefully examined to precisely compute the emitted power.

## Declaration of Competing Interest

None.

## Data availability

Data will be made available on request.

## Acknowledgements

The great datasets recorded and processed by the Cassini ISS, UVIS, and VIMS teams make it possible to conduct the analysis. We also appreciate fruitful discussion with Dr. Andrew Ingersoll on this work. Two anonymous reviewers provided many constructive suggestions, which significantly improve the quality of this manuscript. Finally, we thank for the support from the NASA ROSES Cassini Data Analysis Program (CDAP) and Planetary Data Archiving, Restoration, and Tools (PDART).

## Appendix A. Supplementary data

Supplementary data to this article can be found online at <https://doi.org/10.1016/j.icarus.2023.115429>.

## References

- Ajello, J.M., et al., 2008. Titan airglow spectra from the Cassini ultraviolet imaging spectrograph: FUV disk analysis. *Geophys. Res. Lett.* 35 <https://doi.org/10.1029/2007GL032315>.
- Bevington, P.R., Robinson, D.K., 2003. *Data Reduction and Error Analysis for the Physical Sciences*, 3rd ed. McGraw-Hill.
- Brilliantov, N.V., Schmidt, J., Spahn, F., 2008. Geysers of Enceladus: quantitative analysis of qualitative models. *Planet. Space Sci.* 56, 1596–1606.
- Brown, R.H., et al., 2004. The Cassini visual and infrared mapping spectrometer (VIMS) investigation. *Space Sci. Rev.* 115, 111–168.
- Buratti, B., Veverka, J., 1984. Voyager photometry of Rhea, Dione, Tethys, Enceladus and Mimas. *Icarus* 258, 254–264.
- Buratti, B.J., et al., 2010. Cassini spectra and photometry 0.25–5.1  $\mu\text{m}$  of the small inner moons of Saturn. *Icarus* 206, 524–536.
- Conrath, B.J., Hanel, R.A., Samuelson, R.E., 1989. Thermal Structure and Heat Balance of the Outer Planets. In *Origin and Evolution of Planetary and Satellite Atmospheres*. The University of Arizona Press.
- Creedy, E., Li, L., Jiang, X., West, R., Nixon, C., Fry, P., Kenyon, M., 2021. Titan's global radiant energy budget during the Cassini epoch (2004–2017). *Geophys. Res. Lett.* <https://doi.org/10.1029/2021GL095356>.
- Creedy, E., Li, L., Jiang, X., Fry, P., Nixon, C., West, R., Kenyon, M., 2019. Seasonal variations of Titan's brightness. *Geophys. Res. Lett.* <https://doi.org/10.1029/2019GL084833>.
- Creedy, E., Li, L., Jiang, X., Smith, M.D., Kleinboehl, A., Kass, D.M., Martinez, G., 2022. Mars' emitted energy and seasonal energy imbalance. *PNAS*. <https://doi.org/10.1073/pnas.2121084119>.
- Emery, J.P., Burr, D.M., Cruikshank, D.P., Brown, R.H., Dalton, J.B., 2005. Near-infrared (0.8–4.0  $\mu\text{m}$ ) spectroscopy of Mimas, Enceladus, Tethys, and Rhea. *Astron. Astrophys.* 435, 353–362.
- Esposito, L.W., et al., 2004. The Cassini ultraviolet imaging spectrograph investigation. *Space Sci. Rev.* 115, 299–361.
- Filacchione, G., et al., 2007. Saturn's icy satellites investigated by Cassini-VIMS: I. full-disk properties: 350–5100 nm reflectance spectra and phase curves. *Icarus* 186, 259–290.
- Flasar, F.M., et al., 2004. Exploring the Saturn system in the thermal infrared: the composite infrared spectrometer. *Space Sci. Rev.* 115, 169–297.
- Gioia, G., Chakraborty, P., Marshak, S., Kieffer, S.W., 2007. Unified model of tectonics and heat transport in a frigid Enceladus. *Proc. Natl. Acad. Sci.* 104, 13578–13581.
- Hanel, R., Conrath, B., Flasar, F.M., Kunde, V., Maguire, W., Pearl, J., Pirraglia, J., Samuelson, R., Cruikshank, D., Gautier, D., Gierasch, P., 1982. Infrared observations of the Saturnian system from voyager 2. *Science* 215, 544–548.
- Hanel, R.A., Conrath, B.J., Jennings, D.E., Samuelson, R.E., 2003. Exploration of the Solar System by Infrared Remote Sensing. Cambridge Univ. Press.
- Hansen, C.J., Esposito, L., Stewart, A.I.F., Colwell, J., Hendrix, A., Pryor, W., Shemansky, D., West, R., 2006. Enceladus' water vapor plume. *Science* 311, 1422–1425.
- Hapke, B., 2002. Bidirectional reflectance spectroscopy: 5. The coherent backscatter opposition effect and anisotropic scattering. *Icarus* 157, 523–534.
- Hapke, B., 2012. *Theory of Reflectance and Emittance Spectroscopy*. Cambridge university press.
- Hendrix, A.R., Hansen, C.J., Holsclaw, G.M., 2010. The ultraviolet reflectance of Enceladus: implications for surface composition. *Icarus* 206, 608–617.
- Hendrix, A.R., Filacchione, G., Paranicas, C., Schenk, P., Scipioni, F., 2018. Icy Saturnian satellites: disk-integrated UV-IR characteristics and links to exogenic processes. *Icarus* 300, 103–114.
- Henyey, L.G., Greenstein, J.L., 1941. Diffuse radiation in the galaxy. *Astrophys. J.* 93, 70–83.
- Howett, C.J.A., Spencer, J.R., Pearl, J., Segura, M., 2010. Thermal inertia and bolometric bond albedo values for Mimas, Enceladus, Tethys, Dione, Rhea and Iapetus as derived from Cassini/CIRS measurements. *Icarus* 206, 573–593.
- Howett, C.J.A., Spencer, J.R., Pearl, J., Segura, M., 2011. High heat flow from Enceladus' south polar region measured using 10–600  $\text{cm}^{-1}$  Cassini/CIRS data. *J. Geophys. Res.* 116 <https://doi.org/10.1029/2010JE003718>.
- Knowles, B., et al., 2020. End-mission calibration of the Cassini imaging science subsystem. *Planet. Space Sci.* 185 <https://doi.org/10.1016/j.pss.2020.104898>.
- Lean, J.L., Rind, D.H., 2009. How will Earth's surface temperature change in future decades? *Geophys. Res. Lett.* 36 <https://doi.org/10.1029/2009GL038932>.
- Li, L., et al., 2010. Emitted power of Saturn. *J. Geophys. Res.* 115 <https://doi.org/10.1029/2010JE003631>.
- Li, L., et al., 2011. The global energy balance of Titan. *Geophys. Res. Lett.* 38 <https://doi.org/10.1029/2011GL050053>.
- Li, L., et al., 2012. Emitted power of Jupiter based on Cassini CIRS and VIMS observations. *J. Geophys. Res.* 117 <https://doi.org/10.1029/2012JE004191>.
- Li, L., et al., 2015. Saturn's giant storm and global radiant energy. *Geophys. Res. Lett.* 42 <https://doi.org/10.1002/2015GL063763>.
- Li, L., et al., 2018. Less absorbed solar energy and more internal heat for Jupiter. *Nat. Commun.* <https://doi.org/10.1038/s41467-018-06107-2>.
- McCord, T.B., et al., 2004. Cassini VIMS observations of the Galilean satellites including the VIMS calibration procedure. *Icarus* 172, 104–126.
- McKay, C.P., Porco, C.C., Altheide, T., Davis, W.L., Kral, T.A., 2008. The possible origin and persistence of life on Enceladus and detection of biomarkers in the plume. *Astrobiology* 8, 909–919.
- Mishchenko, M., 1992. The angular width of the coherent backscatter opposition effect - an application to icy outer planet satellites. *Astrophys. Space Sci.* 194, 327–333.
- Mishchenko, M.I., Dlugach, Zh.M., 1992. The amplitude of the opposition effect due to weak localization of photons in discrete disordered media. *Astrophys. Space Sci.* 189, 151–154.
- National Academies of Sciences, Engineering, and Medicine, 2022. *Origins, Worlds, and Life: A Decadal Strategy for Planetary Science and Astrobiology 2023–2032*. The National Academies Press, Washington, DC. <https://doi.org/10.17226/26522>.
- Noll, K.S., Roush, T.L., Cruikshank, D.P., Johnson, R.E., Pendleton, Y.J., 1997. Detection of ozone on Saturn's satellites Rhea and Dione. *Nature* 388, 45–47.
- Pitman, K.M., Buratti, B.J., Mosher, J.A., 2010. Disk-integrated bolometric bond albedo and rotational light curves of saturnian satellites from Cassini visual and infrared mapping spectrometer. *Icarus* 206, 537–560.
- Porco, C.C., et al., 2004. Cassini imaging science: instrument characteristics and anticipated scientific investigations at Saturn. *Space Sci. Rev.* 115, 363–497.
- Porco, C.C., et al., 2006. Cassini observes the active south pole of Enceladus. *Science* 311, 1393–1401.
- Postberg, F., Clark, R.N., Hansen, C.J., Coates, A.J., Dalle Ore, C.M., Scipioni, F., Hedman, M., Waite, J., 2018. Plume and Surface Composition of Enceladus. In: *Enceladus and the Icy Moons of Saturn*. The University of Arizona Space Science Series.
- Spencer, J.R., et al., 2006. Cassini encounters Enceladus: background and the discovery of a south polar hot spot. *science* 311, 1401–1405.
- Spencer, J.R., Nimmo, F., Ingersoll, A.P., Hurford, T.A., Kite, E.S., Rhoden, A.R., Schmidt, J., Howett, C.J.A., 2018. Plume origins and plumbing: from ocean to surface. *Enceladus Icy Moons Saturn* 163–174.
- Thekaekara, M.P., 1973. Solar energy outside the earth's atmosphere. *Sol. Energy* 14, 109–127.
- Verbiscer, A., Helfenstein, P., 1998. Reflectance spectroscopy of icy surfaces. In: *Solar System Ices*. Springer, Dordrecht, pp. 157–197.
- Verbiscer, A.J., Veverka, J., 1990. Scattering properties of natural snow and frost: comparison with icy satellite photometry. *Icarus* 88, 418–428.
- Verbiscer, A.J., Veverka, J., 1994. A photometric study of Enceladus. *Icarus* 110, 155–164.
- Verbiscer, A., Helfenstein, P., Veverka, J., 1990. Backscattering from frost on icy satellites in the outer solar system. *Nature* 347, 162–164.
- Verbiscer, A.J., French, R.G., McGhee, C.A., 2005. The opposition surge of Enceladus: HST observations 338–1022 nm. *Icarus* 173, 66–83.
- Verbiscer, A.J., Peterson, D.E., Skrutskie, M.F., Cushing, M., Helfenstein, P., Nelson, M.J., Smith, J.D., Wilson, J.C., 2006. Near-infrared spectra of the leading and trailing hemispheres of Enceladus. *Icarus* 182, 211–223.
- West, R., et al., 2010. In-flight calibration of the Cassini imaging science sub-system cameras. *Planet. Space Sci.* 58, 1475–1488.
- Willson, R.C., Mordvinov, A.V., 2003. Secular total solar irradiance trend during solar cycles 21–23. *Geophys. Res. Lett.* 30 <https://doi.org/10.1029/2002GL016038>.